RSC Advances

PAPER

View Article Online
View Journal | View Issue

Cite this: *RSC Adv.*, 2025, **15**, 20220

DFT study of free radical scavenging mechanisms in UiO-66-$(OH)_2$ and UiO-66-NH_2 MOFs†

Shuai Ke,[ab] Bo Wang, *[a] Ganggang Liu,[c] Wei Huang,[a] Yubing Gong[a] and Kailin Pan*[a]

This study employs density functional theory (DFT) to investigate three common free radical scavenging mechanisms (hydrogen atom transfer (HAT), single electron transfer proton transfer (SET-PT), and sequential proton loss electron transfer (SPLET)) in UiO-66-$(OH)_2$ and UiO-66-NH_2 metal–organic framework (MOF) nanoparticles under gas, benzene and aqueous phase conditions. The reaction processes between UiO-66-$(OH)_2$/UiO-66-NH_2 and hydroxyl radicals (˙OH) were simulated to elucidate detailed radical capture pathways, and the computational results were validated by macroscopic DPPH radical scavenging experiments. The results indicate that: (1) among the three mechanisms, HAT consistently exhibits the lowest bond dissociation energy across all phases, suggesting MOF nanoparticles preferentially undergo hydrogen atom transfer over electron transfer during radical scavenging; (2) compared to gas phase and nonpolar solvent (benzene), polar solvent (water) significantly lowers the energy barriers for both electron transfer and hydrogen transfer, thus enhancing reactivity across all mechanisms; (3) UiO-66-$(OH)_2$ exhibits a radical scavenging rate constant of 1.0×10^9 M^{-1} s^{-1}, higher than 7.63×10^8 M^{-1} s^{-1} for UiO-66-NH_2; (4) DPPH assays reveal that UiO-66-$(OH)_2$ exhibits an 8% greater radical scavenging efficiency than UiO-66-NH_2, in agreement with DFT predictions and confirming the antioxidative benefit of hydroxyl functionalization. This study proposes a combined DFT and experimental screening workflow for radical scavengers, offering an efficient and economical approach to rapidly identify novel MOF-based radioprotective radical scavengers.

Received 5th March 2025
Accepted 28th May 2025

DOI: 10.1039/d5ra01568e

rsc.li/rsc-advances

1. Introduction

The reliability and service life of aerospace components are significantly affected by long-term exposure to high-energy radiation environments such as protons, electrons, and gamma rays.[1–5] Although inorganic materials such as metals and ceramics dominate due to their extensive applications in the aerospace field, organic polymers are increasingly being utilized in this domain owing to their lightweight properties, excellent processability, and lower cost.[6–9] However, polymers are more sensitive to radiation than metals or inorganic materials.[10–13] Under high-energy radiation, polymer long chains undergo cleavage, generating abundant reactive free radicals (*e.g.*, ˙OH). These radicals readily abstract electrons from adjacent atoms and react to form new chemical bonds, thereby damaging the polymer's microstructure and crosslinking network.[14] This process accelerates the scission of macromolecular chains, ultimately leading to polymer degradation, which significantly reduces the material's mechanical and thermal properties, and severely impacts its service life.[6,15–18] Therefore, eliminating radiation-induced free radicals in polymers is considered a key strategy for enhancing their radiation resistance.

To solve this issue, researchers have tried to incorporate free radical scavengers as fillers to enhance the radiation resistance of polymers.[19–22] However, traditional free radical scavengers based on organic and inorganic nanoparticles often suffer from poor radiation stability, low compatibility with polymers, and limited free radical scavenging efficiency. Metal–organic frameworks (MOFs) are three-dimensional network crystalline materials formed by coordination bonds between organic ligands and inorganic structural units, which is different from traditional organic or inorganic nanoparticles. Their cage-like porous structures and nanoscale channels facilitate the capture of radiation-induced free radicals. Moreover, rich modifiable functional groups of MOFs can capture and neutralize free radicals through various mechanisms, and effectively block free radical chain reactions at the molecular level. In addition, the organic–inorganic hybrid nature of MOFs provides excellent compatibility with polymer matrices, which facilitates high loading capacities and uniform dispersion in composite materials. Zirconium-based MOFs (UiO-66) remain stable even under high-dose gamma radiation of 2 MGy.[23,24]

[a]*Guangxi Key Laboratory of Manufacturing System and Advanced Manufacturing Technology, School of Mechanical and Electrical Engineering, Guilin University of Electronic Technology, Guilin 541004, China. E-mail: wangbo_guet@163.com; pankl@guet.edu.cn*

[b]*Guizhou Equipment Manufacturing Polytechnic, Guiyang 551400, China*

[c]*Guizhou Zhenhua Fengguang Semiconductor Co., Ltd, Guiyang 550018, China*

† Electronic supplementary information (ESI) available. See DOI: https://doi.org/10.1039/d5ra01568e

This is attributed to its strong coordination bonds and the tightly packed atomic arrangement with high bond energy in the secondary building units (SBUs). The exceptional stability of UiO-66 makes it possible to modify functional modifications in a variety of ways, expanding the diversity of its structure and function. Amines and phenols are widely used due to their excellent antioxidant properties. By introducing hydroxyl and amino functional groups on the terephthalate linkers of UiO-66, similar structural features as phenol and aniline were achieved and antioxidant potential was obtained. This makes the material highly reactive in free radical scavenging applications. Wang *et al.* utilized UiO-66-OH nanoparticles as free radical scavengers to delay the degradation of epoxy resin.[25] After high-energy radiation, the long-term free radical content of epoxy resin decreased by 88.17%. However, current research on the mechanisms of MOFs in free radical scavenging is very limited, and the specific roles of different functional groups in scavenging process are still unclear, and need further investigation.

DFT has been proven to be highly effective in elucidating structure–activity relationships, uncovering key antioxidant mechanisms, and interpreting experimental findings.[26–32] Recent studies by Chen, Li, and Zheng employed DFT to systematically investigate radical scavenging in natural cardamonin, phenolamides, and flavonoids.[33–35] These studies proved the significant influence of substituents, non-covalent interactions, carboxyl groups, and solvent effects, while distinguishing the roles of HAT and SPLET pathways across different environments. Combining low computational cost with high accuracy, DFT enables precise prediction of electronic structures, band distributions, and reaction pathways, thereby complementing experimental approaches and guiding rational materials design.

Considering the high cost and lengthy duration of space high-energy radiation experiments, this study proposes an integrated screening strategy combining DFT calculations with ground-based free radical scavenging assays. DFT was employed to investigate the free radical scavenging capabilities of functionalized UiO-66, focusing on the roles of hydroxyl and amino functional groups in radical quenching mechanisms. Key thermodynamic parameters of three common scavenging mechanisms (HAT, SET-PT and SPLET) were computed in both gas and solvent phases, along with kinetic activation energies for the reactions between UiO-66-$(OH)_2$/UiO-66-NH_2 and $^{\bullet}OH$. Based on these computational insights, corresponding radical scavenging experiments were designed using stable radicals that mimic space radiation radicals to validate the DFT predictions and quantitatively assess the radical scavenging efficiency *via* the HAT mechanism. This integrated approach provides a solid theoretical and experimental foundation for subsequent high-energy radiation validation studies.

2. Materials and methods

2.1 Computational detail

All calculations in this study were performed using the DMol^3 module in the Material Studio software. Geometry optimizations and energy calculations were conducted using the spin-polarized density functional theory (DFT) method and the generalized gradient approximation (GGA) with the Perdew–Wang 1991 (PW91) exchange–correlation functional. The treatment of core electrons employed the DFT semi-core pseudopotential.[36] while the atomic orbitals were described using the double numerical plus polarization (DNP) basis set.[37,38] Solvent effects were simulated using the conductor-like screening model (COSMO), and water was used to model solvation effects in nonpolar and polar solutions, respectively. The model treats the solvent as a continuous medium to simulate the polarization effects of solvent molecules on the solute. In the radical calculations, a spin-polarized unrestricted method is employed, allowing independent optimization of different spin orbitals to accurately describe the electron distribution of the radical and its interactions with the solvent. This study employs frontier molecular orbital theory to analyze molecular reactivity and electronic distribution, identifying potential reactive sites. Global descriptors are utilized to evaluate reactivity trends and molecular stability. To elucidate the reaction pathways and mechanisms of radiation-induced free radicals, three radical scavenging pathways are applied, and kinetic analysis is performed to explore the reaction rates and dynamic behavior of the molecule with free radicals.

Given the need to rigorously justify our choice of the PW91 functional and the absence of MOF-specific bond-energy data, we selected phenol (PhOH) and aniline ($PhNH_2$) as representative small molecules. Their O–H and N–H bond dissociation energies (BDEs) were calculated at the PW91/DNP level and benchmarked against authoritative experimental values (see Table S1 in the ESI†). We then validated the transferability of these small-molecule benchmarks to UiO-66 MOF fragments by comparing the relative O–H *versus* N–H bond strengths in both systems. To further ensure the robustness of our findings, we performed a performance comparison using several exchange–correlation functionals and evaluated the effect of dispersion corrections (see Tables S2–S4 in the ESI†).

2.1.1 Frontier molecular orbital analysis. The Frontier Molecular Orbital (FMO) theory states that molecular reactivity is primarily governed by its frontier orbitals, namely the highest occupied molecular orbital (HOMO) and the lowest unoccupied molecular orbital (LUMO).[39] Research has shown that a higher HOMO value indicates a stronger electron-donating ability of antioxidants, whereas a lower LUMO value suggests a stronger electron-accepting ability.[40,41] The HOMO–LUMO energy gap is a critical quantum descriptor reflecting both the electronic orbital transition characteristics and molecular reactivity. Zainuri *et al.* demonstrate that a larger HOMO–LUMO energy gap generally indicates greater kinetic stability and lower reactivity of the molecule, while a smaller energy gap suggests higher reactivity. However, in cases of long-term antioxidant demand, excessively fast reactions of antioxidants may lead to their rapid depletion, resulting in a loss of sustained efficacy.[42] Furthermore, Fazlul *et al.*[43] further indicate that a larger HOMO–LUMO energy gap may confer greater stability and persistence during radical scavenging, thereby offering more long-lasting antioxidant protection.

2.1.2 Global descriptive parameters. Global descriptors of molecules serve as tools for understanding the relationship

between their chemical reactivity, sensitivity to structural perturbations, and responses to changes in external conditions. These descriptors reflect the linear response behavior of electron density to variations in external potential and electron count.[44] Among global descriptors, chemical hardness essentially reflects a molecule's resistance to deformation or polarization of its electron cloud in response to minor perturbations during chemical processes. It serves as an intrinsic measure of a molecule's stability against external disturbances. Chemical softness is a parameter that measures a molecule's ability to accept electrons. It is directly related to the presence of certain specific groups or atoms within the molecule and is inversely proportional to chemical hardness. Electronegativity measures the tendency of a molecule to attract electrons within a chemical bond, making it one of the key indicators of molecular reactivity.[45] Additionally, electrophilicity represents a molecule's ability to accept an electron pair, reflecting its tendency to react with nucleophiles. The electrophilicity index further quantifies the strength of electrophilicity and serves as a critical parameter for predicting a molecule's behavior in chemical reactions.[46,47] The calculation formulas for global descriptors, including electronegativity χ, hardness η, softness S, electrophilicity ω, and the electrophilicity index ω_i, are as follows:

Electronegativity (χ) was calculated from the following equation:

$$\chi = (E_{HOMO} + E_{LUMO})/2 \quad (1)$$

Hardness (η) was calculated from the following equation:

$$\eta = (E_{LUMO} - E_{HOMO})/2 \quad (2)$$

Electrophilicity (ω) was calculated from the following equation:

$$\omega = ((E_{HOMO} + E_{LUMO})/2)^2/2\eta \quad (3)$$

Softness (S) was calculated from the following equation:

$$S = 1/2\eta \quad (4)$$

Electrophilicity index (ω_i) was calculated from the following equation:

$$\omega_i = \mu^2/2\eta \quad (5)$$

2.1.3 Reaction path analysis. Compounds containing amino and hydroxyl functional groups typically exert their antioxidant effects through the following three common mechanisms: HAT, SET-PT, and SPLET.[48,49] Fig. 1 illustrates schematic diagrams of the three mechanisms.

(1) HAT mechanism:

$$ArOH \rightarrow Aro^{\cdot} + H^{\cdot} \quad (6)$$

$$BDE = H_{H\cdot} + H_{ArOH\cdot} - H_{ArOH} \quad (7)$$

where $H_{ArO\cdot}$, $H_{H\cdot}$, and H_{ArOH} represent the enthalpy of the compound radical, the hydrogen atom, and the compound, respectively.

(2) SET mechanism:

$$ArOH \rightarrow ArOH^{+\cdot} + e^- \quad (8)$$

$$IP = H_{ArOH^{+\cdot}} + H_{e^-} - H_{ArOH} \quad (9)$$

$$ArOH^{+\cdot} \rightarrow ArO^{\cdot} + H^+ \quad (10)$$

$$PDE = H_{ArO\cdot} + H_{H^+} - H_{ArOH^{+\cdot}} \quad (11)$$

H_{e^-}, $H_{ArOH^{+\cdot}}$, H_{H^+} represent the enthalpy of the electron, the proton-free radical, and the proton, respectively.

(3) SPLET mechanism:

$$ArOH \rightarrow ArO^- + H^+ \quad (12)$$

$$PA = H_{ArO^-} + H_{H^+} - H_{ArOH} \quad (13)$$

$$ArO^- \rightarrow ArO^{\cdot} + e^- \quad (14)$$

$$ETE = H_{ArO\cdot} + H_{e^-} - H_{ArO^-} \quad (15)$$

H_{ArO^-} represent the enthalpy of the anion.

2.1.4 Reaction kinetics analysis. The quantum mechanics-based overall free radical scavenging activity (QM-ORSA) method is used to predict the kinetic parameters of radical reactions. The accuracy of this method has been validated by experimental results.[50–53] The rate constant (k) of the reaction is calculated based on Transition State Theory (TST), with the specific formula shown below:

$$K = \sigma\kappa\frac{K_B T}{h}e^{(-\Delta G^{\neq})/RT} \quad (16)$$

where σ represents the reaction symmetry number, k_B is the Boltzmann constant, T is the temperature (298.15 K), h is the Planck constant, and κ is the tunneling correction factor calculated using the Wigner method. $\Delta G^{\neq}$ is the Gibbs free energy of activation.

2.2 Experimental

2.2.1 Materials. *N*,*N*-Dimethylformamide (DMF), aceticacid (CH_3COOH), ethanol, zirconium(IV) chloride ($ZrCl_4$), 2,5-

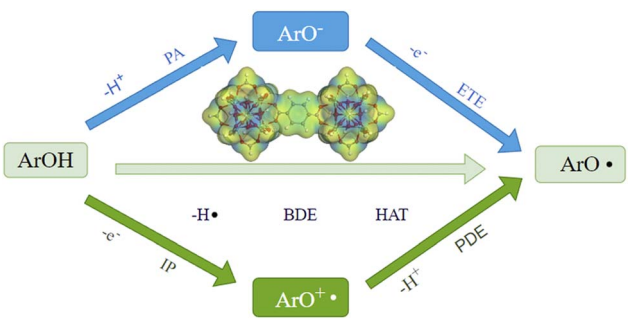

Fig. 1 Schematic diagram of the three mechanisms.

dihydroxyterephthalic acid ($H_2BDC\text{-}(OH)_2$) and 2-amino-terephthalic acid ($H_2BDC\text{-}NH_2$) were purchased from commercial suppliers and used as received without further purification.

2.2.2 Preparation of UiO-66-$(OH)_2$ and UiO-66-NH_2 nanoparticles. UiO-66-NH_2 was synthesized *via* a solvothermal method as follows. 0.2466 g of $H_2BDC\text{-}NH_2$ was dissolved in 9.4 mL of DMF under vigorous stirring for 15 min. Then 2.3 mL of acetic acid was added dropwise to promote nucleation. In parallel, 0.318 g of $ZrCl_4$ was dissolved in 9.4 mL of DMF with stirring for 30 min. The two solutions were combined, stirred for another 20 min, transferred to a Teflon-lined autoclave, and heated at 120 °C for 24 h. The resulting precipitate was collected by centrifugation (5000 rpm, 30 min), washed three times with 100 mL portions of ethanol, and then freeze-dried under vacuum at −60 °C for 3 h to yield UiO-66-NH_2. UiO-66-$(OH)_2$ was prepared identically, substituting $H_2BDC\text{-}NH_2$ with $H_2BDC\text{-}(OH)_2$.

2.2.3 Characterization. Field-emission scanning electron microscopy (FE-SEM) was employed to investigate the surface morphology and particle size distribution of UiO-66-$(OH)_2$ and UiO-66-NH_2. Samples were prepared by dispersing the as-synthesized nanoparticles in acetone, sonicating for 3 h, and depositing a drop of the suspension onto a pre-cleaned silicon wafer, followed by air drying. Phase purity and crystallinity were evaluated by powder X-ray diffraction (XRD) using Cu Kα radiation over a 2θ range of 5−80°.

2.2.4 Assay for antioxidant activities of UiO-66-$(OH)_2$/UiO-66-NH_2 particles. DPPH (2,2-diphenyl-1-picrylhydrazyl) is a stable nitrogen-centered free radical with a strong absorption peak at 517 nm wavelength of light, which can be used to measure radical scavenging activity *via* Ultraviolet-visible Spectroscopy (UV-vis).[54] The DPPH radical scavenging assay not only quantitatively evaluates the antioxidant activity but also reflects the ability of antioxidants to scavenge free radicals through the HAT mechanism. The UiO-66-$(OH)_2$ and UiO-66-NH_2 nanoparticles were each redispersed in an appropriate solvent and subjected to ultrasonication to yield homogeneous stock suspensions. Working solutions at 6.25, 12.5, 25, 50, 100, 125, 150, 175, and 200 μg mL^{-1} were prepared in ethanol (to account for the differing molecular weights of the two MOFs-such that equal mass corresponds to unequal molar amounts-the UiO-66-NH_2 data were normalized to molar concentration). In each assay, 2 mL of 0.1 mmol per L DPPH solution was mixed with 2 mL of sample and allowed to react in the dark for 30 min. After the reaction, the absorbance at 517 nm was recorded on a UV-vis spectrophotometer (UV-2700; scan rate 2 nm s^{-1}; 300−800 nm), and radical scavenging efficiency was calculated. All measurements were performed in triplicate, and mean values were reported.

The calculation formula for the radical scavenging efficiency is as follows:

$$\text{DPPH scavenging ratio}(\%) = \frac{A_{\text{standard}} - (A_{\text{mixture}} - A_{\text{blank}})}{A_{\text{standard}}} \times 100 \quad (17)$$

where A_{standard} represents the standard absorbance of the DPPH solution without the free radical scavenger, A_{mixture} refers to the absorbance of the mixed solution after adding the free radical scavenger, and A_{blank} denotes the background absorbance of the solution after adding the free radical scavenger.[55] UV-vis measurements were conducted using a UV-2700 spectrophotometer (scanning rate 2 nm s^{-1}, wavelength range: 300–800 nm). SEM analysis was conducted with a Hitachi S4800, and XRD analysis was performed with an Empyrean PIXcel3D (Cu Kα, $\lambda = 1.5406$ Å, 2θ range 5°–80°).

3. Result and discussion

3.1 Optimization of stable structure

The computational models in this study were derived from the experimentally determined UiO-66 crystal structure (CCDC

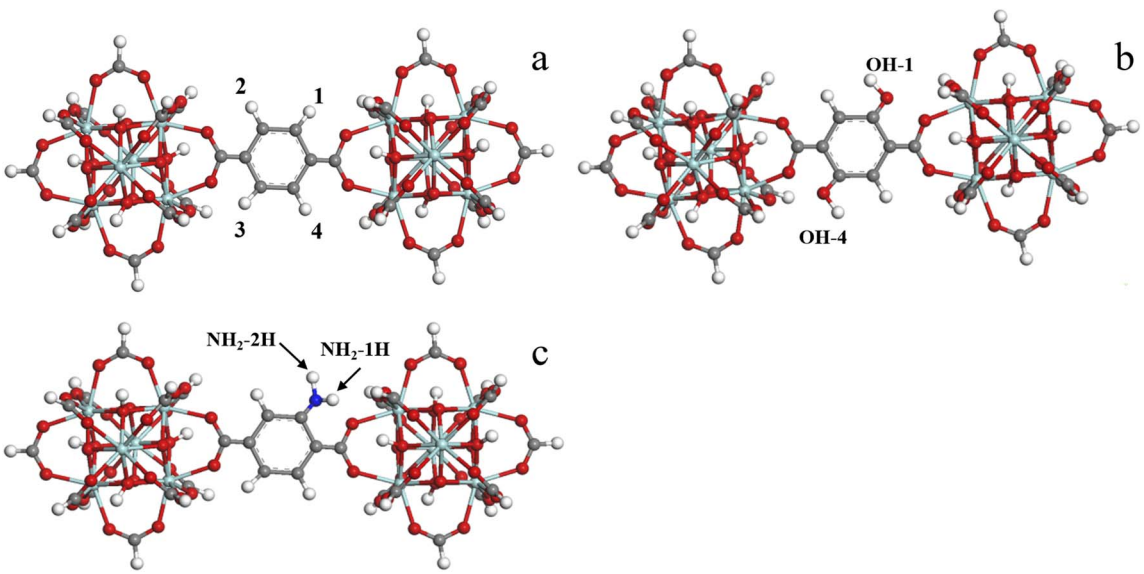

Fig. 2 Stable structure of (a) UiO-66; (b) UiO-66-$(OH)_2$; (c)UiO-66-NH_2; Zr, C, O, N, and H atoms are represented by blue-gray, gray, red, blue, and white spheres, respectively.

database), which features two Zr-oxide secondary building units bridged by benzene-1,4-dicarboxylate linkers (Fig. 2a).[38] To generate finite clusters amenable to nonperiodic DFT, all undercoordinated Zr and O atoms at the truncation boundaries were capped with hydrogen atoms, yielding Zr–H and O–H termini that restore full valency. The convergence criteria for the optimization process were set as follows: energy convergence threshold of 2.0×10^{-4} Ha, force convergence threshold of 0.02 Ha $Å^{-1}$, and atomic displacement convergence threshold of 0.05 Å. During optimization, all atoms in the model, including the passivating hydrogen atoms, were allowed to relax freely without any constraints until convergence was achieved. Analysis of the model's geometry reveals the absence of ideal mirror-plane or rotational symmetries (*e.g.*, C_2 or D_2h point groups), mono-functionalized clusters possess four symmetry-inequivalent substitution sites (H1–H4), and di-functionalized clusters present two unique patterns (H1–H3 and H2–H4). After optimizing all possible conformers, a Maxwell–Boltzmann analysis at 298 K revealed that the lowest-energy conformer accounts for over 99% of the population (Table 1), confirming its dominance. The final optimized geometries (Fig. 1b and c) show that both $–NH_2$ and –OH substituents remain coplanar with the benzene linker and induce negligible distortion of the inorganic–organic framework. These findings demonstrate that functionalization preserves the system's conjugation and structural integrity.

Hydrogen bonds have a significant impact on free radical scavenging activity. According to the studies by Steiner and Desiraju.[56,57] The recommended geometric parameters for hydrogen bonds are as follows: the distance between the hydrogen atom and the acceptor atom (H–A) should be less than 3.0 Å, and the donor–hydrogen–acceptor (D–H–A) angle should be greater than 110° to ensure effective formation and stability of the hydrogen bond. The size parameters of the organic linkers in UiO-66 do not fully meet the typical requirements for hydrogen bonding, resulting in a lower probability of hydrogen bond formation. For details, please refer to Fig. S1 and Table S5 in the ESI.† With the introduction of amino and hydroxyl groups, the probability of hydrogen bond formation increases. In the hydroxyl-functionalized structure, the O2–H2 bond length is 2.307 Å, and the C2–H2···O2 angle is 100.192°. Although the bond length and angle are not entirely ideal, there is still a possibility of weak hydrogen bond formation. In the amino functionalized structure, the O1–H1 distance is only 1.919 Å, and the angle N–H1···O1 is 128.848° (greater than 110°), indicating the presence of a relatively strong hydrogen bond. Subsequent thermodynamic and kinetic calculations revealed anomalous changes in the parameters of this region, further confirming the existence of hydrogen bonding, which plays a significant role in the structural stability and free radical scavenging ability.

Table 1 Relative energies (kcal mol^{-1}) and population percentages (%) at 298 K, calculated using the Maxwell–Boltzmann distribution for amino-and hydroxyl-functionalized UiO-66 derivatives

Functional group type	Substitution position	Relative energy (kcal mol^{-1})	Population ratio
$–NH_2$	1	0	99.472%
	2	3.46	0.290%
	3	4.36	0.063%
$–(OH)_2$	4	3.76	0.175%
	1, 3	0	99.418%
	2, 4	3.05	0.582%

3.2 Molecular orbital and molecular electrostatic potential analysis

Frontier molecular orbitals (FMO) is a vital molecular parameter for free radical scavenging potential.[58] Fig. 3 shows the HOMO and LUMO energy levels of UiO-66-NH_2 and UiO-66-$(OH)_2$, along with their energy gap (ΔE = LUMO − HOMO) and Molecular Electrostatic Potentials (MEP). The HOMO and LUMO are primarily concentrated on the organic linker part, while the metal cluster is unaffected. This indicates that the organic linker is more reactive than the metal cluster, and the amino and hydroxyl groups on the ligand benzene ring modulate the electronic properties of the molecule, potentially serving as reactive sites in chemical reactions. The HOMO and LUMO values of UiO-66-$(OH)_2$ (−5.7 eV, −3.3 eV) are both lower than those of UiO-66-NH_2 (−4.9 eV, −3.0 eV). These changes in energy levels are caused by the hydroxyl group being a stronger electron-withdrawing group, which more effectively stabilizes negative charges, whereas the amino group exhibits a relatively stronger electron-donating ability. By calculating the molecular orbital energy gap (ΔE = LUMO − HOMO), it was found that the ΔE of UiO-66-$(OH)_2$ is 2.4 eV, while that of UiO-66-NH_2 is 1.9 eV. A higher energy gap indicates greater chemical stability and relatively lower reactivity, while a lower energy gap may lead to higher reaction rates and lower stability. Although the lower ΔE of UiO-66-NH_2 suggests potentially better reactivity, the overall reaction activity is still influenced by factors such as intermolecular hydrogen bonding and the local electronic environment.

MEP is typically presented in the form of electrostatic potential maps, which display information about the shape and location of the electrostatic potential on the molecule. It can also identify favorable sites for nucleophilic and electrophilic attacks, helping to predict and explain the reactivity of the molecule.[59] As shown in Fig. 3, the red regions, located on the hydrogen atoms of the amino and hydroxyl groups on the organic linker at both ends of the cluster, represent negative charges and are prone to reacting with electrophilic reagents. The blue regions, located near the oxygen atoms in the cluster, represent positive charges and are more susceptible to nucleophilic attack. In phenolic compounds, the hydroxyl group, due to its higher electrostatic potential, becomes the primary site for electrophilic attack, exhibiting strong antioxidant activity. MEP analysis shows that UiO-66 hydroxyl and amino derivatives display similar electronic properties, suggesting that they also have potential free radical scavenging ability.

3.3 Global reactive descriptors

Table 2 shows the global descriptor parameters of UiO-66-$(OH)_2$ and UiO-66-NH_2 obtained from calculations. The chemical

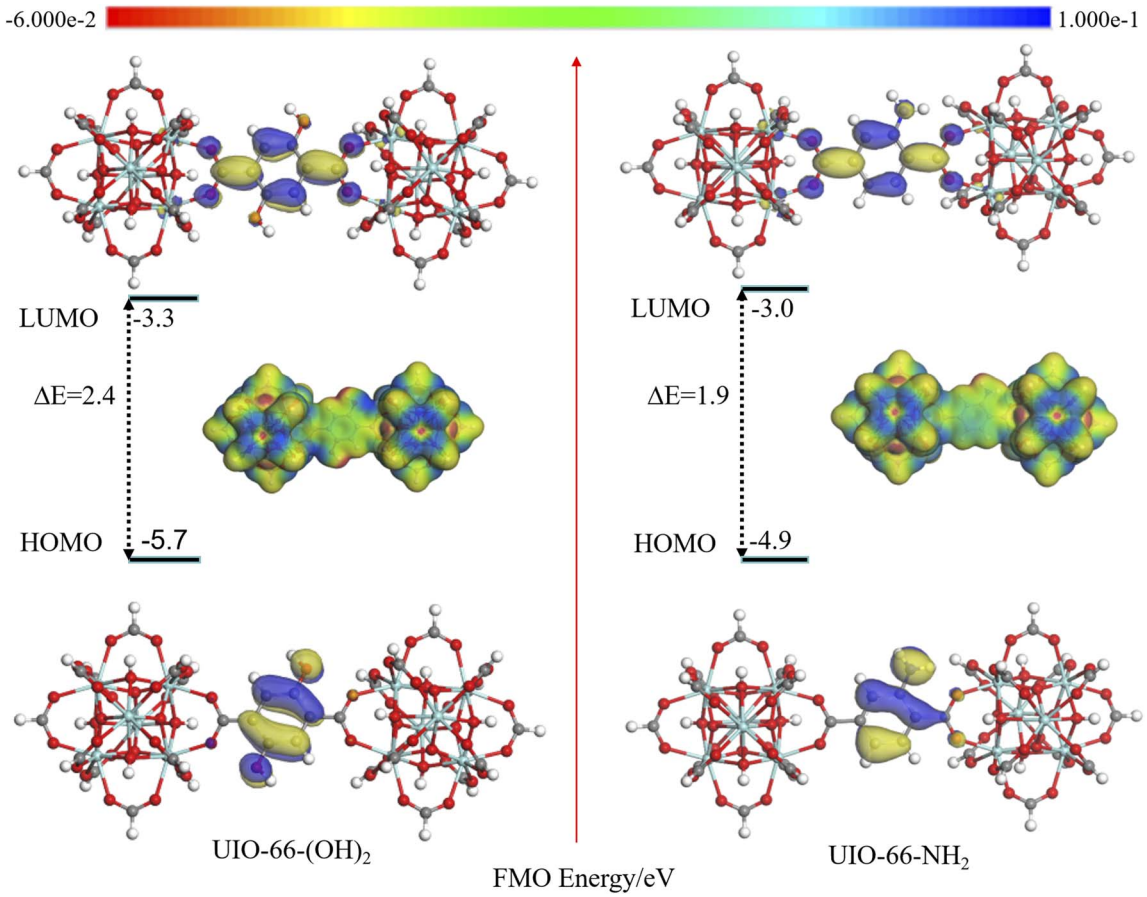

Fig. 3 The frontier molecular orbitals (FMO) and molecular electrostatic potential (MEP) maps of UiO-66-$(OH)_2$ and UiO-66-NH_2 calculated in the gas phase. The units are in electron volts (eV), with red representing electron-rich sites and blue representing electron-deficient sites.

hardness of UiO-66-$(OH)_2$ (1.2245) is higher than that of UiO-66-NH_2 (0.9524), indicating its greater stability and ability to more effectively stabilize and capture free radicals. Moreover, the electronegativity (−4.4899), electrophilicity (16.4544), and electrophilic index (8.2276) of UiO-66-$(OH)_2$ are all higher than those of UiO-66-NH_2 (electronegativity: −3.9457, electrophilicity: 16.3376, electrophilic index: 8.1698), respectively, indicating stronger electron-withdrawing and electrophilic abilities, and greater reactivity. In contrast, the softness of UiO-66-NH_2 is 0.5251, higher than that of UiO-66-$(OH)_2$ (0.4083), suggesting potentially greater reactivity and adaptability in certain reactions. However, its lower hardness and electrophilicity limit its overall activity and stability.

Overall, the electronic structure of UiO-66-NH_2 is more susceptible to external influences, which makes it somewhat deficient in stability and long-term antioxidative capability. In contrast, UiO-66-$(OH)_2$ demonstrates superior overall antioxidant performance and chemical stability.

3.4 Analysis of radical scavenging reaction paths

3.4.1 BDE: HAT pathway indicator. HAT can neutralize free radicals by transferring the hydrogen atom from the hydroxyl or amino group, and is one of the key mechanisms through which phenolic and amino antioxidants exert their effects. In this mechanism, bond dissociation energy (BDE) serves as an indicator of antioxidant activity, with lower BDE values indicating that hydrogen abstraction reactions are more likely to occur, and the compound exhibits higher free radical scavenging ability.

Table 3 shows the BDE values of UiO-66-NH_2 and UiO-66-$(OH)_2$ in the gas phase and solvent phases (benzene and water). The BDE values in different media range from 88.02 to

Table 2 Global descriptor parameters of UiO-66-NH_2 and UiO-66-$(OH)_2$

Compound	Electronegativity (χ)	Hardness (η)	Electrophilicity (ω)	Softness (S)	Electrophilicity index (ω_i)
UiO-66-$(OH)_2$	−4.4899	1.2245	16.4544	0.4083	8.2276
UiO-66-NH_2	−3.9457	0.9524	16.3376	0.5251	8.1698

Table 3 BDE values of the Analyzed Compounds in the gas phase and solvents

	BDE (kcal mol^{-1})		
Comp/position	Gas	Benzene	Water
UiO-66-(OH)$_2$			
OH-1	94.82	91.19	86.91
OH-4	95.60	91.39	88.02
UiO-66-NH$_2$			
NH$_2$-1H	110.21	109.51	108.32
NH$_2$-2H	103.98	103.81	103.26

110.21 kcal mol^{-1}. In both the gas phase and solvent phases, the BDE of UiO-66-NH$_2$ is generally higher than that of UiO-66-(OH)$_2$. These values and trends are consistent with those of phenolic and amine compounds reported in the literature.[34]

In the gas, benzene, and water phases, the average BDE values of UiO-66-(OH)$_2$ are 95.21, 91.29, and 87.47 kcal mol^{-1}, respectively, all lower than those of UiO-66-NH$_2$ (107.10, 106.66, and 105.79 kcal mol^{-1}). This indicates that UiO-66-(OH)$_2$ is more easily able to abstract a hydrogen atom in HAT. Overall, the BDE values decrease from the gas phase to the water phase, suggesting that solvation, particularly in polar solvents, weakens hydrogen bonds and reduces the energy required for homolytic bond dissociation. This is because increasing solvent polarity weakens intramolecular hydrogen bonds within molecules. In polar solvents, solvent molecules can compete with the hydroxyl and amino groups for hydrogen bonding, thereby weakening these intramolecular interactions. This competitive effect facilitates the dissociation of hydroxyl and amino groups, making them more prone to homolytic cleavage. A similar phenomenon has also been observed in previous studies.[60]

The hydroxyl substitution shows a lower BDE value than the amino substitution, as the phenoxyl radical formed after hydrogen abstraction has a lower and more stable energy. The difference in BDE values between the hydroxyl groups at the 1 and 4 positions is because the metal clusters at both ends of the model and the central organic linker are not aligned in a straight line but instead form an angle of 161°. This angle causes the hydroxyl group on one side to be closer to the oxygen in the metal cluster, resulting in the formation of more weak hydrogen bonds. The average BDE difference between the amino groups at positions 1 and 2 in the three phases is 5.66 kcal mol^{-1}, which is higher than the average difference of 0.69 kcal mol^{-1} for the hydroxyl groups at positions 1 and 4 in the three phases. This may be attributed to the relatively consistent electronic environment of the two hydroxyl groups, whereas the amino group is influenced by intramolecular hydrogen bonding.

3.4.2 IP and PDE: SET-PT pathway indicators. SET-PT is an important antioxidant mechanism to describe electron and proton transfer processes. This mechanism is characterized by ionization potential (IP) and proton dissociation enthalpy (PDE), where lower IP and PDE values indicate stronger electron-donating properties and easier electron and proton transfer, suggesting better free radical scavenging activity.[61] Table 4 lists the calculated IP and PDE values associated with the SET-PT mechanism in different media.

IP is an important indicator of electron-donating ability. Molecules with lower IP values are generally more likely to donate electrons. The data in the table show that the IP values of UiO-66-(OH)$_2$ in the gas phase, benzene phase, and water phase are 168.31, 149.32, and 110.56 kcal mol^{-1}, respectively, while the IP values of UiO-66-NH$_2$ are 165.48, 145.92, and 108.94 kcal mol^{-1} in the same phases. The differences in the same phases are 2.83, 3.40, and 1.62 kcal mol^{-1}, respectively. These differences are primarily due to the distinct electronic distribution and interaction mechanisms of the amino and hydroxyl groups. The nitrogen atom in the amino group, with its lone pair of electrons, can effectively conjugate with the π-electron system of the benzene ring, exhibiting electron-donating properties. In contrast, the oxygen atom in the hydroxyl group, due to its higher electronegativity, shows electron-withdrawing characteristics, which results in the amino group having a slightly stronger electron-donating ability than the hydroxyl group. Solvation significantly affects the IP values. The average IP values of UiO-66-(OH)$_2$ and UiO-66-NH$_2$ in the gas, benzene, and water phases are 166.89, 147.62, and 109.75 kcal mol^{-1}, respectively. In both benzene and water phases, the IP values are reduced by approximately 19.3 and 57.1 kcal mol^{-1} compared to the gas phase. The substantial decrease in the IP values in the polar water phase indicates that the cationic radicals are more stable in polar media. Solvent plays a crucial role in modulating the SET-PT mechanism, which contrasts with BDE, as BDE shows lower sensitivity to solvent polarity.[34] These results are in line with previous studies.[62]

PDE is an important parameter in the second step of the SET-PT mechanism. It measures the tendency of the free radical cation formed in the first step to undergo deprotonation. Table 4 shows that in the gas phase, IP < PDE for all sites, while in the solvent phase, IP > PDE for all sites. This indicates that in the gas phase, proton release from the free radical cation is more difficult than electron transfer from the neutral species, whereas in the solvent phase, the reverse is true. Furthermore, the PDE values for all sites decrease sequentially from the gas phase to the water phase, with the maximum average deviation between the gas and water phases reaching 223.87 kcal mol^{-1}. These results suggest that solvation effects, particularly in polar solvents, significantly promote the deprotonation of free radical

Table 4 IP and PDE values of compounds in the gas phase and solvents

	IP (kcal mol^{-1})			PDE (kcal mol^{-1})		
Compounds	Gas	Benzene	Water	Gas	Benzene	Water
UiO-66-(OH)$_2$	168.31	149.32	110.56			
OH-1				243.69	38.07	18.79
OH-4				244.61	38.42	19.72
UiO-66-NH$_2$	165.48	145.92	108.94			
NH$_2$-1H				265.44	61.19	43.62
NH$_2$-2H				259.24	54.39	37.01

cations. The overall energy requirement for the SET-PT mechanism is determined by the sum of IP and PDE. The minimum energy required for UiO-66-$(OH)_2$ and UiO-66-NH_2 in this mechanism are 129.35 and 145.95 kcal mol^{-1}, respectively, both significantly higher than the minimum energy requirements under the BDE mechanism (86.91 and 103.26 kcal mol^{-1}, respectively). This indicates that the HAT mechanism is thermodynamically more favorable compared to SET-PT. This result is consistent with previous studies.[63]

3.4.3 PA and ETE: SPLET pathway indicators. SPLET involves two main steps: deprotonation and subsequent electron transfer.[64] The potential of the SPLET mechanism is explored using the descriptors Proton Affinity (PA) and Electron Transfer Enthalpy (ETE). Smaller PA and ETE values indicate that the antioxidant is more likely to release protons and transfer electrons, thereby enhancing its efficiency in scavenging free radicals.[49]

Table 5 shows that in all studied environments, the PA value of UiO-66-$(OH)_2$ is lower than that of UiO-66-NH_2, indicating its stronger deprotonation ability. In the gas, benzene, and water phases, the PA values gradually decrease, with the average PA values in the benzene and water phases reduced by 231.08 and 280.42 kcal mol^{-1}, respectively, compared to the gas phase. This indicates that the solvent plays a significant role in promoting deprotonation, with polar solvents being more favorable for this process than non-polar solvents. This is because polar solvents, compared to non-polar solvents, have a higher dielectric constant, which can more effectively stabilize the anion formed during deprotonation.

The ETE values in the table range from 75.3 to 89.56 kcal mol^{-1}, with very small differences, especially within the same functional group, where the average deviation is only 0.70 kcal mol^{-1} (for hydroxyl) and 0.62 kcal mol^{-1} (for amino). This indicates that the type and position of the functional group have little impact on the ETE value. This is primarily due to the rigid structure of the MOFs framework, which leads to changes in local substitution sites that do not significantly affect the overall electron distribution. Additionally, the similar polarity of hydroxyl and amino groups results in similar behavior during the electron transfer process. However, the ETE values in solution are slightly higher than those in the gas phase, which is attributed to the fact that the solvation enthalpy of the anion is greater than that of the electron and neutral radical. This phenomenon is consistent with previous reports.[63,65]

Table 5 PA and ETE values of compounds in the gas phase and solvents

	PA (kcal mol^{-1})			ETE (kcal mol^{-1})		
Compounds	Gas	Benzene	Water	Gas	Benzene	Water
UiO-66-$(OH)_2$						
OH-1	332.88	99.32	47.36	79.47	89.03	81.88
OH-4	332.97	98.18	48.04	80.53	89.56	82.38
UiO-66-NH_2						
NH_2-1H	348.17	120.26	72.84	76.05	85.68	77.86
NH_2-2H	342.71	114.67	66.80	75.30	85.57	78.86

In the SPLET mechanism, the total energy requirement of the reaction is determined by (PA + ETE). The average values of (PA + ETE) in the gas phase, benzene phase, and aqueous phase are 417.02, 195.57, and 139.51 kcal mol^{-1}, respectively. The energy requirement in the aqueous phase is significantly lower than that in the gas and benzene phases, indicating that the SPLET mechanism has a distinct advantage in aqueous environments and is more likely to dominate the reaction pathway. This is in excellent agreement with results obtained from similar polyphenols.[63] Notably, the electron transfer enthalpy (ETE) is the only thermodynamic and kinetic parameter that shows better performance for UiO-66-NH_2 compared to UiO-66-$(OH)_2$, which may be related to the strong hydrogen bonding interactions of the amino functional group and its electronic structure.

3.5 Reaction kinetics study

The hydroxyl radical exhibits strong oxidizing properties and is one of the most reactive radicals due to its unpaired electron. Under high-energy radiation (such as γ-rays or electrons), polymers generate $^{\bullet}$OH radicals, which initiate chain degradation reactions, leading to molecular chain scission and severe damage to the material's properties. To further understand the details of free radical trapping, this study employs transition state theory (TST) to investigate the reaction pathway and calculates the kinetic parameters of the optimal mechanism HAT at 298.15 K to better understand its reaction characteristics.

Table 6 shows the kinetic and thermodynamic parameters of the reactions between different sites of UiO-66-$(OH)_2$ and UiO-66-NH_2 with $^{\bullet}$OH, and all calculations performed under gas-phase conditions. As shown in the table, the activation free energies of the four sites are similar, ranging from 4.13 to 5.72 kcal mol^{-1}, with an average activation free energy of 4.63 kcal mol^{-1}, which indicates a low reaction barrier, making the reaction easily achievable. This conclusion is consistent with the findings from studies on polyphenolic compounds in similar reactions.[66] The Gibbs free energies of the OH-1 site in UiO-66-$(OH)_2$ and the NH_2-2H site in UiO-66-NH_2 are −16.51 and −13.00 kcal mol^{-1}, respectively, indicating that these reactions are exothermic. In contrast, the Gibbs free energies of the OH-4 site in UiO-66-$(OH)_2$ and the NH_2-1H site in UiO-66-NH_2 are 7.80 and 10.86 kcal mol^{-1}, respectively, suggesting that these reactions are endothermic. These differences may be

Table 6 Gibbs free energies of activation ($\Delta G^{\neq}$) and reaction (ΔG), along with rate constants (k) for the reactions of UiO-66-NH_2/UiO-66-$(OH)_2$ with $^{\bullet}$OH *via* the HAT mechanism in the gas phase at 298.15 K

Comp/position		$\Delta G^{\neq}$ (kcal mol^{-1})	ΔG (kcal mol^{-1})	k (M^{-1} s^{-1})
UiO-66-$(OH)_2$	OH-1	4.13	−16.51	1.00×10^{9}
	OH-4	5.72	7.80	6.83×10^{7}
UiO-66-NH_2	NH_2-1H	4.29	10.86	7.63×10^{8}
	NH_2-2H	4.36	−13.00	6.78×10^{8}

related to the strength and distribution of hydrogen bonds. Additionally, the reaction rate of the OH-1 site is $1.00 \times 10^9\ M^{-1}\ s^{-1}$, the highest among all reaction sites, indicating its significant hydrogen-donating ability and highest reactivity, which is consistent with the thermodynamic calculation results.

Fig. 4 shows the optimized transition state (TS) structures. In the TS of UiO-66-$(OH)_2$, the partially broken H···O bond lengths (1.756 Å and 1.752 Å) are shorter than the newly formed H···O bond lengths (2.028 Å and 1.982 Å), indicating that hydrogen transfer is still in the early stage and that the TS geometry remains closer to that of the reactants. In contrast, in the TS of UiO-66-NH_2, the bond lengths being broken (1.865 Å and 1.292 Å) are longer than those being formed (1.759 Å and 1.190 Å), suggesting that this TS is more product-like. This difference may be attributed to the higher electronegativity of hydroxyl groups, which favors retaining the original H···O bonding structure during the transition state, thereby conferring greater initial stability and a geometry closer to the reactants. In contrast, because amino groups exhibit weaker electron-withdrawing capabilities, they more readily undergo bond reorganization, making the TS more product-like. Such differences give rise to the distinct TS geometries of UiO-66-$(OH)_2$ and UiO-66-NH_2, ultimately affecting their kinetic pathways. This finding highlights the crucial role of molecular substituents in modulating the electronic distribution and geometry of transition states, offering new insights into substituent effects on reaction kinetics.

4. Overall antioxidant activity experiments

DFT results indicate that hydrogen atom transfer (HAT) is the most favorable mechanism among the three radical scavenging pathways studied. The DPPH generates persistent active radicals that serve as a preliminary model for radiation-induced free radicals encountered in space environments, predominantly reflecting the antioxidant efficiency *via* the HAT mechanism. Therefore, the DPPH assay was employed to experimentally validate the antioxidant activity in this study.

4.1 Nanoparticle characterization

The UiO-66-$(OH)_2$ and UiO-66-NH_2 nanoparticles were dispersed in acetone solution, and their morphological characteristics are shown in Fig. 5(a) and (b). Both nanoparticles exhibit similar morphology, displaying nearly octahedral shapes with an average particle size of approximately 200 nm and a uniform size distribution. Fig. 5(c) shows the XRD experimental and simulated patterns of the two nanoparticles. The experimental patterns match well with the simulated ones, and the characteristic peaks at 2θ correspond to the crystal planes reported in the literature.[67]

4.2 Free radical analysis

The DPPH free radical scavenging activity of the nanoparticles was plotted based on experimental results. Fig. 6(a) shows the free radical scavenging rates of four types of nanoparticles (UiO-66-$(OH)_2$, UiO-66-NH_2, graphene oxide (GO), carbon nanotubes (CNTs)), which initially increase monotonically with the particle concentration before leveling off. Fig. 6(b) presents the maximum free radical scavenging rates of four types of nanoparticles. The free radical scavenging rate of UiO-66-$(OH)_2$ is 63%, which is notably higher than that of UiO-66-NH_2 (56%). Additionally, these values exceed those reported in the literature for graphene oxide (39%) and carbon nanotubes (36%).[25] This could be attributed to the superior free radical scavenging mechanisms of UiO-66-$(OH)_2$ and UiO-66-NH_2, along with the high surface area and cage-like structure of MOFs, which also contribute to effective radical capture. MOFs have unique

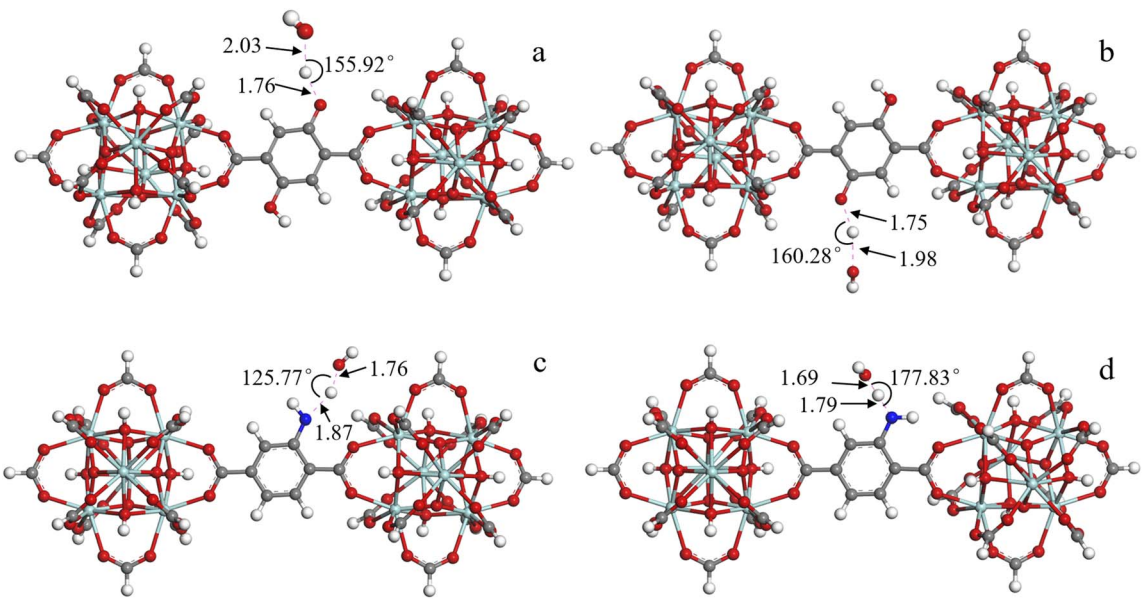

Fig. 4 Shows the transition state structures of the reaction between UiO-66-$(OH)_2$ and UiO-66-NH_2 with $^{\bullet}OH$, including (a) OH-1, (b) OH-4, (c) NH_2-1H, and (d) NH_2-2H.

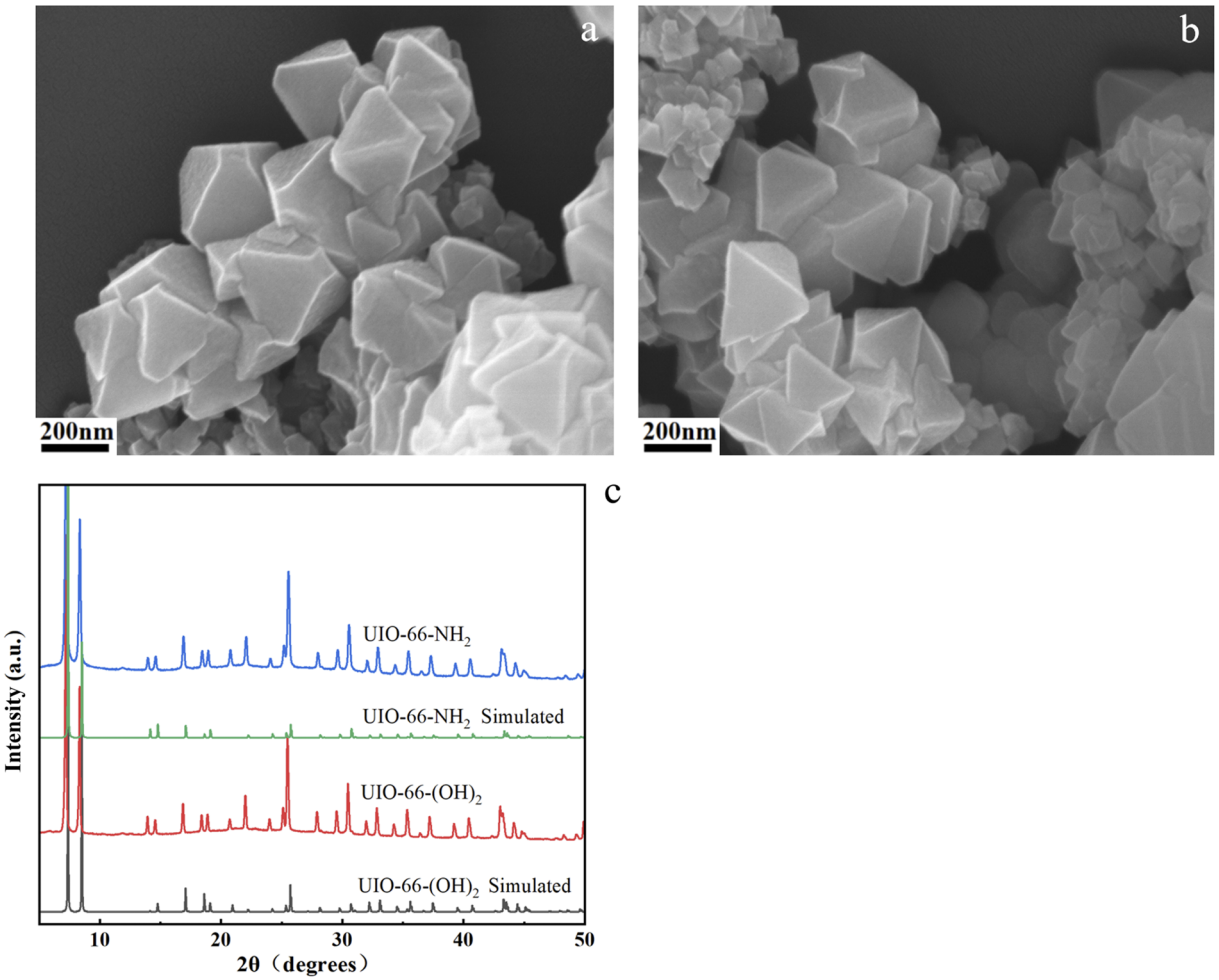

Fig. 5 (a and b) SEM of UiO-66-$(OH)_2$ and UiO-66-NH_2; and (c) XRD experimental and simulated patterns of UiO-66-$(OH)_2$ and UiO-66-NH_2.

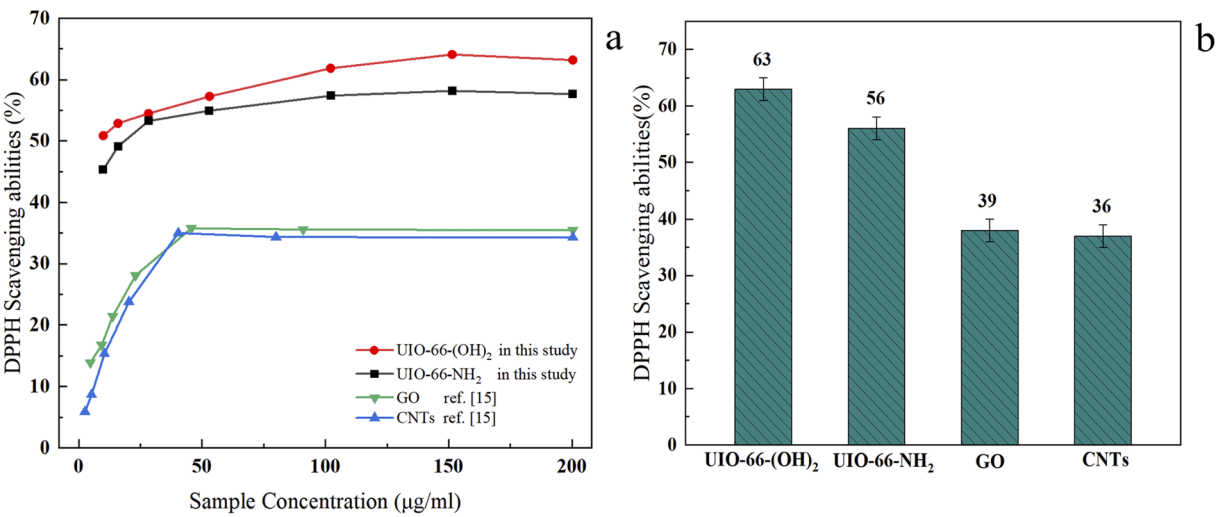

Fig. 6 (a) DPPH radical scavenging ratios of UiO-66-$(OH)_2$, UiO-66-NH_2, GO, and CNTs nanoparticles at varying concentrations. (b) Maximum free radical scavenging rates of the four nanoparticles.

advantages in free radical scavenging, effectively capturing radiation-induced free radicals in polymers and enhancing their radiation stability.

As shown in Fig. 7, this study has established a "DFT calculation + radical scavenging experiments" strategy for the screening of radical scavengers. The process consists of three

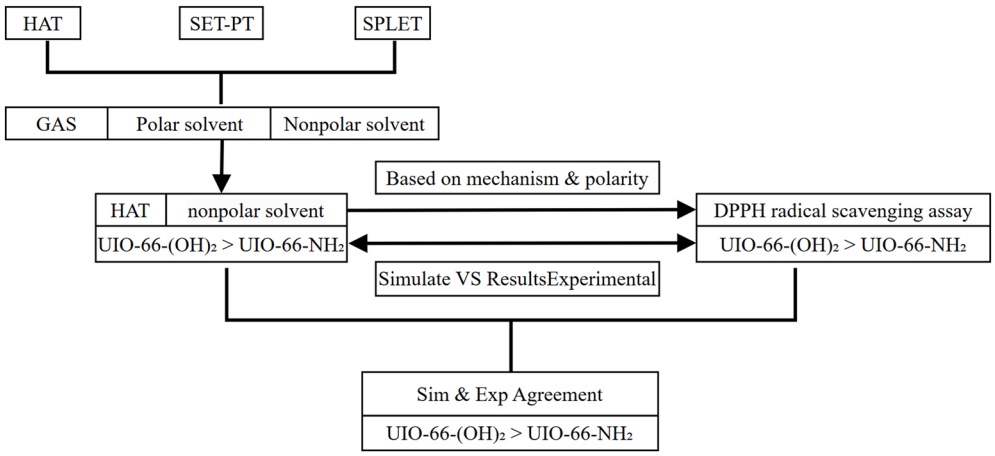

Fig. 7 Workflow of the "DFT calculations + DPPH assays" screening strategy for free radical scavengers.

main stages: (1) DFT calculations were used to determine the reaction energy barriers of UiO-66-$(OH)_2$ and UiO-66-NH_2 for three radical scavenging mechanisms (HAT, SET-PT, SPLET) in the gas, benzene and aqueous phase, and preliminarily evaluate the radical scavenging ability and characteristics of the two; (2) based on the dominant mechanism predicted by DFT, the relevant DPPH radical scavenging experiments were selected for verification and analysis; (3) the calculation and experimental results were combined to select the candidate materials with the highest radical scavenging efficiency.

The excellent agreement between DPPH assays and DFT predictions confirms the reliability of this integrated approach. Given the high cost and lengthy timelines of actual radiation tests, our rapid, cost-effective screening protocol provides a practical route for the preliminary identification of advanced MOF-based radioprotectors.

5. Conclusion

The study investigated the radical scavenging capabilities of UiO-66-$(OH)_2$ and UiO-66-NH_2 based on DFT and analyzed the thermodynamic parameters of three common radical scavenging mechanisms and the dynamic characteristics of their transition states. The radical scavenging abilities are further validated through DPPH experiments. The main conclusions are as follows:

(1) The energy optimization and Maxwell–Boltzmann distribution results show that both UiO-66-$(OH)_2$ and UiO-66-NH_2 exhibit a single-phase structure, with strong hydrogen bonding present in UiO-66-NH_2.

(2) Molecular properties (HOMO/LUMO) and global descriptors indicate that UiO-66-$(OH)_2$ outperforms UiO-66-NH_2 in environmental resistance, chemical stability, and long-term antioxidant capacity.

(3) Among all the studied environments, HAT is a more active mechanism with lower energy cost compared to SET-PT and SPLET, and UiO-66-$(OH)_2$ exhibits a greater thermodynamic advantage over UiO-66-NH_2.

(4) The kinetic results of the reaction between the nanoparticles and $^{\bullet}OH$ radicals show that the reaction barriers for all four reaction sites are low, with a small difference, and the maximum being only 1.59 kcal mol^{-1}, indicating that these sites exhibit similar reaction activities kinetically.

Overall, MOF nanoparticles, with their high specific surface area and ease of functional group modification, exhibit significant potential in free radical scavenging. Further investigation into their radical scavenging mechanisms could aid in optimizing the design of radiation-resistant materials, thereby enhancing their application potential in radiation protection.

Data availability

The authors confirm that the data supporting the findings of this study are available within the article and/or its ESI.†

Conflicts of interest

There are no conflicts to declare.

Acknowledgements

National Natural Science Foundation of China (U2441249); Natural Science Foundation of Guangxi Province (2025GXNSFBA069011); Guangxi Key Laboratory of Manufacturing System and Advanced Manufacturing Technology (23354S009); Project for Enhancing Young and Middle-aged Teacher's Research Basis Ability in Colleges of Guangxi (2024KY0220).

References

1 Q. Yu, P. Chen, Y. Gao, K. Ma, C. Lu and X. Xiong, *Nucl. Instrum. Methods Phys. Res., Sect. B*, 2014, **336**, 158–162.
2 Y. Zhang, Z. Sun, Y. Yu, J. Guo, F. Fang, Y. Zhou, Z. Wang, Y. Zhang and B. Hu, *Nucl. Instrum. Methods Phys. Res., Sect. A*, 2020, **971**, 164112.

3 J. H. Lee, H. N. Kim, H. Y. Jeong and S. O. Cho, *Nucl. Eng. Technol.*, 2020, **52**, 1817–1825.
4 M. Bricout, C. Onofri, A. Debelle, Y. Pipon, R. C. Belin, F. Garrido, F. Lepretre and G. Gutierrez, *J. Nucl. Mater.*, 2020, **531**, 1–10.
5 C. Hu, F. Yang, L. Zhang, R. Y. Zhu, J. Kapustinsky, M. Mocko, R. Nelson and Z. Wang, *IEEE Trans. Nucl. Sci.*, 2020, **67**, 1086–1092.
6 F. Diao, Y. Zhang, Y. Liu, J. Fang and W. Luan, *Nucl. Instrum. Methods Phys. Res., Sect. B*, 2016, **383**, 227–233.
7 A. S. Putra, S. Huo and L. Smith, *Composites, Part A*, 2023, **160**, 107241.
8 A. Q. Dayo, L. L. Zhang, J. Wang, W. B. Liu, S. Kiran, A. Zegaoui, H. A. Ghouti and Y. B. Arse, *J. Appl. Polym. Sci.*, 2020, **137**, 48313.
9 A. Zegaoui, A. R. Wang, A. Q. Dayo, B. Tian, W. B. Liu, J. Wang and Y. G. Liu, *Radiat. Phys. Chem.*, 2017, **141**, 110–117.
10 A. Bedar, P. K. Tewari, R. C. Bindal and S. Kar, *Appl. Surf. Sci.*, 2020, **507**, 144897.
11 A. M. Schmalzer, C. M. Cady, D. Geller, D. O. Acosta, A. T. Zocco, J. Stull and A. Labouriau, *Radiat. Phys. Chem.*, 2017, **130**, 103–111.
12 A. Canel, H. Korkut and T. Korkut, *Radiat. Phys. Chem.*, 2019, **158**, 13–16.
13 J. Kim, S. J. Pearton, C. Fares, J. C. Yang, F. Ren, S. Kim and A. Y. Polyakov, *J. Mater. Chem. C*, 2019, **7**, 10–24.
14 M. Marrale, A. Longo, S. Panzeca, S. Gallo, F. Principato, E. Tomarchio, A. Parlato, A. Buttafava, D. Dondi and A. Zeffiro, *Nucl. Instrum. Methods Phys. Res., Sect. B*, 2014, **339**, 15–19.
15 Y. Lin, Y. Liu, D. Zhang, C. Chen and G. Wu, *Chem. Eng. J.*, 2017, **315**, 516–526.
16 L. Hou, Y. Wu, J. Xiao, B. Guo and Y. Zong, *Polym. Degrad. Stab.*, 2019, **166**, 8–16.
17 M. R. Kaçal, F. Akman, M. I. Sayyed and F. Akman, *Nucl. Eng. Technol.*, 2019, **51**, 818–824.
18 J. Lv, H. Wang, J. Xu, Y. Liu, H. Zhang, J. Sun, H. Zhao and C. Zhu, *Chem. Lett.*, 2019, **48**, 426–428.
19 G. Audran, S. Dorey, N. Dupuy, F. Gaston and S. R. A. Marque, *Polym. Degrad. Stab.*, 2015, **122**, 169–179.
20 N. J. AbuAlRoos, N. A. Baharul Amin and R. Zainon, *Radiat. Phys. Chem.*, 2019, **165**, 108439.
21 W. Xia, H. Xue, J. Wang, T. Wang, L. Song, H. Guo, X. Fan, H. Gong and J. He, *Carbon*, 2016, **101**, 315–323.
22 M. Yan, L. Liu, L. Chen, N. Li, Y. Jiang, Z. Xu, M. Jing, Y. Hu, L. Liu and X. Zhang, *Composites, Part B*, 2019, **172**, 447–457.
23 J. Hajek, M. Vandichel, B. V. D. Voorde, B. Bueken, D. D. Vos, M. Waroquier and V. V. Speybroeck, *J. Catal.*, 2015, **331**, 1–12.
24 C. Volkringer, C. Falaise, P. Devaux, R. Giovine, V. Stevenson, F. Pourpoint, O. Lafon, M. Osmond, C. Jeanjacques, B. Marcillaud, J. C. Sabroux and T. Loiseau, *Chem. Commun.*, 2016, **52**, 12502–12505.
25 S. Wang, L. Song, S. Liu, X. Pei, Y. Zhao, C. Min, R. Shao, T. Ma, Y. Yin, Z. Xu and C. Wang, *Polym. Degrad. Stab.*, 2023, **207**, 110231.
26 G. Wang, Y. Liu, L. Zhang, L. An, R. Chen, Y. Liu, Q. Luo, Y. Li, H. Wang and Y. Xue, *Food Chem.*, 2020, **304**, 125446.
27 Y. Xue, Y. Teng, M. Chen, Z. Li and G. Wang, *J. Agric. Food Chem.*, 2021, **69**, 7178–7189.
28 A. Purushothaman, K. S. T. Rose, J. M. Jacob, R. Varatharaj, K. Shashikala and D. Janardanan, *Food Chem.*, 2022, **373**, 131499.
29 A. Amic, Z. Markovic, J. M. D. Markovic, D. Milenkovic and V. Stepanic, *Phytochemistry*, 2020, **170**, 112218.
30 Y. Z. Zheng, Y. Zhou, R. Guo, Z. M. Fu and D. F. Chen, *LWT-Food Sci. Technol.*, 2020, **120**, 108932.
31 Y. Shang, X. Li, Z. Li, J. Zhou, L. Qu and K. Chen, *Food Chem.*, 2022, **378**, 131975.
32 L. Yang, H. Liu, D. Xia and S. Wang, *Molecules*, 2020, **25**, 1192.
33 M. Chen, Z. Li, G. Sun, S. Jin, X. Hao, C. Zhang, L. Liu, L. Zhang, H. Liu and Y. Xue, *Phytochemistry*, 2023, **207**, 113580.
34 Z. Li, G. Sun, M. Chen, S. Jin, X. Hao, C. Zhang, J. Ouyang, J. Zhu, B. Li, F. Cheng and Y. Xue, *J. Mol. Liq.*, 2023, **383**, 122140.
35 Y. Zheng, G. Deng and Y. Zhang, *Dyes Pigm.*, 2022, **198**, 109877.
36 J. M. Herbert, *Wiley Interdiscip. Rev.: Comput. Mol. Sci.*, 2022, **12**, e1547.
37 S. H. Çetinkaya, E. Öztürk and M. R. Şener, *J. Mol. Model.*, 2019, **25**, 37–46.
38 W. Sun, H. Li, H. Li, S. Li and X. Cao, *Chem. Eng. J.*, 2019, **360**, 645–653.
39 E. Brémond and C. Adamo, *J. Comput. Chem.*, 2021, **42**, 1285–1302.
40 S. M. R. Nazifi, M. H. Asgharshamsi, M. M. Dehkordi and K. K. Zborowski, *Free Radical Res.*, 2019, **53**, 922–931.
41 K. Akhtari, K. Hassanzadeh, B. Fakhraei, N. Fakhraei, H. Hassanzadeh and S. A. Zarei, *Comput. Theor. Chem.*, 2013, **1013**, 123–129.
42 D. A. Zainuri, I. A. Razak and S. Arshad, *Acta Crystallogr., Sect. E: Crystallogr. Commun.*, 2018, **74**, 1427–1432.
43 H. Fazlul, *J. Pharmacol. Toxicol.*, 2007, **2**, 176–182.
44 V. K. Rajan and K. Muraleedharan, *Food Chem.*, 2017, **220**, 93–99.
45 S. Wang and G. Yang, *Chem. Rev.*, 2015, **115**, 4893–4962.
46 K. Srivastava, S. Srivastava and M. T. Alam, *Int. J. Innov. Appl. Res.*, 2014, **2**, 19–34.
47 V. K. Rajan, C. K. Hasna and K. Muraleedharan, *Food Chem.*, 2018, **262**, 184–190.
48 Y. Xue, Y. Zheng, L. An, Y. Dou and Y. Liu, *Food Chem.*, 2014, **151**, 198–206.
49 A. D. T. Fouegue, H. Tedongmo, R. A. Ntieche and J. N. Ghogomu, *J. Phys. Org. Chem.*, 2021, **34**, e4245.
50 A. Galano and J. R. A. Idaboy, *J. Comput. Chem.*, 2013, **34**, 2430–2445.
51 A. Galano and J. R. A. Idaboy, *Int. J. Quantum Chem.*, 2019, **119**, e25665.
52 J. Shi, L. Zhang and Z. Cheng, *J. Catal. Sur. Asia.*, 2021, **25**, 279–300.

53 E. Vélez, J. Quijano, R. Notario, E. Pabón, J. Murillo, J. Leal, E. Zapata and G. Alarcón, *J. Phys. Org. Chem.*, 2009, **22**, 971–977.
54 A. Chinthamreddy, R. Karreddula, G. K. Pitchika and M. S. SurendraBabu, *J. Inorg. Organomet. Polym. Mater.*, 2021, **31**, 1381–1394.
55 Y. Wang, M. F. Li, L. Wang, J. Tan, R. Li, Z. T. Jiang, S. H. Tang and T. T. Li, *J. Sci. Food Agric.*, 2021, **101**, 287–296.
56 T. Steiner, *Angew. Chem., Int. Ed.*, 2002, **41**, 48–76.
57 G. R. Desiraju, *Acc. Chem. Res.*, 1996, **29**, 441–449.
58 S. H. Çetinkaya, E. Öztürk and M. R. Şener, *J. Mol. Model.*, 2019, **25**, 37–46.
59 S. Molaei, A. D. Tehrani and H. Shamlouei, *J. Mol. Liq.*, 2023, **377**, 121506.
60 N. Nenadis and M. P. Sigalas, *Food Res. Int.*, 2011, **44**, 114–120.
61 Y. Z. Zheng, G. Deng, D. F. Chen, Q. Liang, R. Guo and Z. M. Fu, *Food Chem.*, 2018, **240**, 323–329.
62 N. M. Thong, Q. V. Vo, T. L. Huyen, M. V. Bay, D. Tuan and P. C. Nam, *ACS Omega*, 2019, **4**, 14996–15003.
63 Y. Shang, H. Zhou, X. Li, J. Zhou and K. Chen, *New J. Chem.*, 2019, **43**, 15736–15742.
64 Y. Xue, Y. Zheng, L. An, Y. Dou and Y. Liu, *Food Chem.*, 2014, **151**, 198–206.
65 Y. Xue, Y. Liu, Q. Luo, H. Wang, R. Chen, Y. Liu and Y. Li, *J. Phys. Chem. A*, 2018, **122**, 8520–8529.
66 Q. V. Vo, M. V. Bay, P. C. Nam and A. Mechler, *J. Phys. Chem. B*, 2019, **123**, 7777–7784.
67 M. R. DeStefano, T. Islamoglu, S. J. Garibay, J. T. Hupp and O. K. Farha, *Chem. Mater.*, 2017, **29**, 1357–1361.